



Diffuse optical tomography with the impulse stripe illumination and the depth of the banana

Manabu Machida, Keita Osada & Keiichiro Kagawa

To cite this article: Manabu Machida, Keita Osada & Keiichiro Kagawa (2024) Diffuse optical tomography with the impulse stripe illumination and the depth of the banana, Journal of Modern Optics, 71:4-6, 135-149, DOI: [10.1080/09500340.2024.2400193](https://doi.org/10.1080/09500340.2024.2400193)

To link to this article: <https://doi.org/10.1080/09500340.2024.2400193>



© 2024 The Author(s). Published by Informa UK Limited, trading as Taylor & Francis Group.



Published online: 08 Sep 2024.



Submit your article to this journal [↗](#)



Article views: 141



View related articles [↗](#)



View Crossmark data [↗](#)

Diffuse optical tomography with the impulse stripe illumination and the depth of the banana

Manabu Machida^a, Keita Osada^b and Keiichiro Kagawa^c

^aDepartment of Informatics, Faculty of Engineering, Kindai University, Higashi-Hiroshima, Japan; ^bGraduate School of Integrated Science and Technology, Shizuoka University, Hamamatsu, Japan; ^cResearch Institute of Electronics, Shizuoka University, Hamamatsu, Japan

ABSTRACT

Diffuse optical tomography with impulse stripe illumination is investigated. The stripe illumination lies between the illumination in the spatial-frequency domain and the point illumination. Although the stripe illumination has a periodic structure as the illumination in the spatial-frequency domain, light from the stripe illumination can reach deep regions in biological tissue since it can be regarded as an array of point illuminations. We perform diffuse optical tomography for the stripe illumination against forward data taken by Monte Carlo simulation. We consider an impulse illumination of the shape of a stripe. We propose a numerical scheme for this time-resolved measurement and the absorption coefficient of a target is reconstructed. To obtain insight about the pitch of stripes, we investigate the depth of the banana shape. In general, the depth depends on the absorption and diffusion coefficients, and the ratio of refractive indices on the boundary.

ARTICLE HISTORY

Received 5 November 2023
Accepted 23 August 2024

KEYWORDS

Diffuse light; optical tomography; stripe illumination; time-domain measurements

1. Introduction

Conventionally in diffuse optical tomography, light has been illuminated and detected with optical fibres [1]. For example, with optical fibres 96 source and 92 detector positions were used for diffuse optical tomography to investigate the brain function [2]. Noncontact diffuse optical tomography can be achieved when a laser beam is sent to a sample to which no optical fibre is attached and the detected light is measured by a CCD or CMOS camera [3,4]. As an alternative noncontact diffuse optical tomography, measurements in the spatial frequency domain has been proposed [5] (see [6,7] and references therein). Spatially oscillating light makes wide field illumination possible [8].

When the measurement is performed in the spatial frequency domain, the penetration depth of near-infrared light can be controlled by the spatial frequency. Light with high spatial frequencies can reach shallow regions and is reflected back to the surface of the sample. In other words, spatially oscillating light cannot reach deep regions compared with a planar light which uniformly illuminates the surface or a pencil beam which is illuminated at a point on the surface.

A natural question is that if there exists a method which overcomes weaknesses for both the point illumination and spatially oscillatory illumination. To answer

this question, in this paper, we consider diffuse optical tomography with the stripe illumination. Since the stripe illumination can be regarded as the illumination with multiple spatial frequencies (a stripe illumination can be expressed as the sum of illuminations of multiple spatial frequencies.), on one hand, it is the measurement in the spatial frequency domain. On the other hand, the stripe illumination can be regarded as an array of point illuminations. Hence the stripe illumination acts as a bridge between measurements in the real spatial domain and spatial frequency domain. Moreover, we perform measurements in time domain by sending an impulse of near-infrared light for the stripe illumination and use the time-resolved measurement data [9].

For the conventional near-infrared measurement of one point illumination and one point detection [10,11], trajectories of the detected light in the sample are known to form a banana shape [12–17]. In this paper, we consider the depth of the banana, which gives insight for the pitch of stripes. We found that the depth of the centre of the banana is about 0.2 of the source–detector distance for typical measurements for biological tissue with the Fresnel reflection on the surface.

The remainder of this paper is organized as follows. In Section 2, the impulse stripe illumination is introduced. In Section 3, we obtain tomographic images for

CONTACT Manabu Machida  machida@hiro.kindai.ac.jp  Department of Informatics, Faculty of Engineering, Kindai University, Higashi-Hiroshima 739-2116, Japan

the forward data computed by Monte Carlo simulation. Results are shown in Section 4. Concluding remarks are given in Section 5. In Appendix 1, we consider the banana shape for diffuse light. Furthermore, results from Monte Carlo simulation are shown in Appendix 2, the Green's function was derived in Appendix 3, Appendix 4 is devoted to the computation of H_ω , which is introduced in (27) below, and the regularized pseudoinverse is discussed in Appendix 5.

2. Impulse stripe illumination

Let $\mathbf{r} = (\boldsymbol{\rho}, z)$ be a vector in \mathbb{R}^3 , where $\boldsymbol{\rho} \in \mathbb{R}^2$ is a vector in the $x-y$ plane. Let Ω be the half-space ($z > 0$):

$$\Omega = \left\{ \mathbf{r} \in \mathbb{R}^3; -\infty < x < \infty, -\infty < y < \infty, 0 < z < \infty \right\}. \quad (1)$$

Let $\partial\Omega$ be the boundary of Ω , i.e. the $x-y$ plane. Suppose that Ω is occupied by a medium in which near-infrared light propagates. The outside $\mathbb{R}^3 \setminus \bar{\Omega}$ is air.

Let c_0 be the speed of light in vacuum. Then $c = c_0/n$ is the speed of light in the medium. Let $T > 0$ be the observation time. The diffuse fluence rate $u(\mathbf{r}, t)$ for the impulse illumination obeys the following diffusion equation [18]:

$$\begin{cases} \frac{1}{c} \frac{\partial}{\partial t} u - D_0 \Delta u + \mu_a(\mathbf{r})u = f, & (x, t) \in \Omega \times (0, T), \\ -D_0 \frac{\partial}{\partial z} u + \frac{1}{\zeta} u = 0, & (x, t) \in \partial\Omega \times (0, T), \\ u = 0, & \mathbf{r} \in \Omega, \quad t = 0, \end{cases} \quad (2)$$

where $f(\mathbf{r}, t)$ is the incident beam. Here, $\bar{\mu}_a > 0$ is the absorption coefficient and $D_0 = 1/(3\mu'_s)$ is the diffusion coefficient with μ'_s the reduced scattering coefficient. We assume the diffuse surface reflection and give the constant ζ by [19]

$$\zeta = 2 \frac{1+R}{1-R}, \quad R = -1.4399n^{-2} + 0.7099n^{-1} + 0.6681 + 0.0636n, \quad (3)$$

where n is the ratio of the refractive indices inside and outside the medium. We note that R in (3) is the internal diffuse surface reflectance. For example, $\zeta \approx 6.50$ when $n = 1.4$. We refer the reader to [20,21] for the boundary conditions of diffuse light.

In Section 3, we will write the absorption coefficient $\mu_a(\mathbf{r})$ as

$$\mu_a(\mathbf{r}) = \bar{\mu}_a + \delta\mu_a(\mathbf{r}), \quad (4)$$

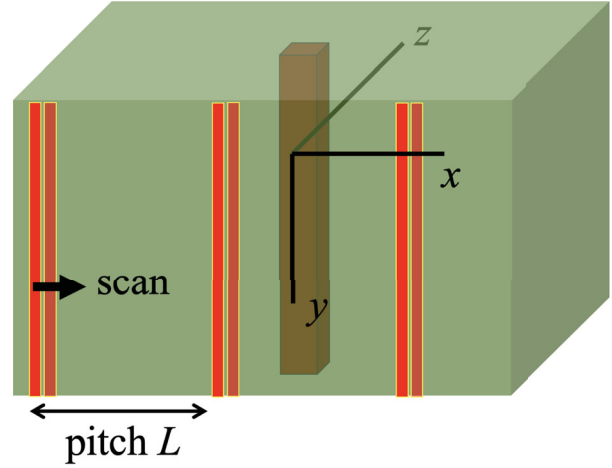


Figure 1. Schematic figure (top view) for the stripe illumination of pitch L (shown as three red rectangles). The same illumination pattern is scanned in the positive x direction with step ℓ . The absorption inhomogeneity $\delta\mu_a(\mathbf{r})$ shown in the domain is the absorption bar assumed in Section 3. In the $x-z$ plane, the bar has four corners at $(-6, 4)$, $(-6, 10)$, $(0, 4)$ and $(0, 10)$ in the unit of mm.

where $\bar{\mu}_a$ is a positive constant. We assume that $\mu_a|_{\partial\Omega} = \bar{\mu}_a$. The source term $f(\mathbf{r}, t)$ is given by

$$f(\mathbf{r}, t) = f_0 s(\boldsymbol{\rho}) \delta(t) \delta(z), \quad (5)$$

where $f_0 > 0$ is a constant. On the right-hand side, $\delta(\cdot)$ is the Dirac delta function. Let L, ℓ be the pitch and scan step, respectively. A schematic figure of the illumination is shown in Figure 1. Since the width of each stripe is much smaller than the spacing (pitch L) of stripes, we model the stripes using the Dirac delta function. That is, stripe illumination is expressed as a comb of delta functions with spacing L . Each of such a comb takes N_f different positions. Thus the function $s(\boldsymbol{\rho})$ is given by

$$s(\boldsymbol{\rho}) = s_n(\boldsymbol{\rho}) = \sum_{j=-\infty}^{\infty} \delta\left(x - jL - \frac{2n-1}{2}\ell\right), \quad (6)$$

where $n = 1, \dots, N_f$ and N_f is the number of scans. In Section 3, we set

$$L = 32 \text{ mm}, \quad \ell = 2 \text{ mm}, \quad N_f = 16. \quad (7)$$

Let us define

$$p_l = \frac{2\pi l}{L}, \quad l \in \mathbb{Z}. \quad (8)$$

Then the function $s_n(\boldsymbol{\rho})$ can be written as

$$s_n(\boldsymbol{\rho}) = \frac{1}{L} \sum_{l=-\infty}^{\infty} e^{ip_l x} e^{-ip_l(2n-1)\ell/2}, \quad (9)$$

where we used the Poisson sum formula

$$\sum_{j=-\infty}^{\infty} \delta(x - 2\pi j) = \frac{1}{2\pi} \sum_{l=-\infty}^{\infty} e^{ilx}. \quad (10)$$

The expression (9) implies that the solution to (2) can be expressed as

$$u(\mathbf{r}, t) = \sum_{l=-\infty}^{\infty} u_l(\mathbf{r}, t), \quad (11)$$

where u_l ($l = -\infty, \dots, \infty$) is the solution of (2) for

$$f(\mathbf{r}, t) = f_l(\mathbf{r}, t) = \frac{f_0}{L} e^{ip_l x} e^{-ip_l(2n-1)\ell/2} \delta(t) \delta(z). \quad (12)$$

We will discuss in the end of Appendix 1, for constant μ_a , it is known that the penetration depth (i.e. the decay rate of $u(\mathbf{r})$ in the z -direction) depends on the spatial frequency p_l . We have asymptotically [6,22]

$$u_l(\mathbf{r}, t) \sim \text{const.} \times e^{-z\sqrt{\mu_{\text{eff}}^2 + p_l^2}}, \quad (13)$$

where

$$\mu_{\text{eff}} = \sqrt{3\mu_a(\mu_a + \mu'_s)}. \quad (14)$$

Since u is given by the sum of u_l in (11), the diffuse light u penetrates deeper than the light by a single sinusoidal illumination.

3. Diffuse optical tomography

The forward data were taken numerically for diffuse optical tomography. For this purpose, the Monte Carlo eXtreme (MCX) was used [23]. The number of photons used in each simulation was 10^8 . In our numerical experiment by Monte Carlo simulation, an absorption bar ($\mu_a = 0.02 \text{ mm}^{-1}$, $\mu_s = 10 \text{ mm}^{-1}$, $g = 0.9$ ($\mu'_s = 1 \text{ mm}^{-1}$)) is embedded in Ω along the y -axis. The cross-section of the bar is parallel to the $x-z$ plane and is a square of side length 6 mm. The depth of the centre of the square is 7 mm. In the $x-z$ plane, the positions of four corners of the absorber rectangle are $(-6, 4)$, $(-6, 10)$, $(0, 4)$ and $(0, 10)$ in the unit of mm. In the depth direction along the z -axis, the absorption bar exists in $4 \text{ mm} \leq z \leq 10 \text{ mm}$ (Figure 1). The Monte Carlo simulation was performed in a box ($-64 \leq x \leq 64 \text{ mm}$, $-64 \leq y \leq 64 \text{ mm}$, $0 \leq z \leq 40 \text{ mm}$) with voxel size $2 \text{ mm} \times 2 \text{ mm} \times 2 \text{ mm}$. The Robin boundary condition is considered on the illumination plane (i.e. according to the Fresnel reflection a part of outgoing photons reenters the

medium instead of exiting it). The zero boundary condition is imposed on other boundaries. In the medium, we set

$$\bar{\mu}_a = 0.01 \text{ mm}^{-1}, \quad \mu'_s = 1 \text{ mm}^{-1}, \quad n = 1.4. \quad (15)$$

We remark that the target shape in the y -direction is assumed to be known in this optical tomography. That is, $\delta\mu_a$ is independent of y and the reconstruction in the $x-z$ plane will be performed. The target depth is deeper than the depth typically assumed in spatial frequency domain imaging [5].

To obtain reconstructed images for the impulse stripe illumination, we propose a numerical scheme of taking the Fourier transform both for time and spatial variables.

Let us extend the interval $(0, T)$ to $(-\infty, \infty)$ by the limit $T \rightarrow \infty$ and zero extension for $t < 0$, we consider the Fourier transform as

$$v^n(\mathbf{r}, \omega) = \int_{-\infty}^{\infty} e^{-i\omega t} u(\mathbf{r}, t) dt \quad (16)$$

for $n = 1, \dots, N_f$. We note that the unit of time is picosecond in the simulation.

We have

$$\begin{cases} -D_0 \Delta v^n + (\alpha(\omega) + \delta\mu_a(\mathbf{r})) v^n & x \in \Omega, \\ = f_0 a_n(\boldsymbol{\rho}) \delta(z), & \\ -D_0 \frac{\partial}{\partial z} v^n + \frac{1}{\zeta} v^n = 0, & x \in \partial\Omega, \end{cases} \quad (17)$$

where

$$\alpha(\omega) = \bar{\mu}_a + \frac{i\omega}{c}. \quad (18)$$

We note that $\delta\mu_a(\mathbf{r})$ is nonzero in the volume of the bar, whose position is described in the beginning of this section. In the bar, $\delta\mu_a(\mathbf{r})$ takes the constant value of 0.01.

Let us consider the Green's function $G_\omega(\mathbf{r}, \mathbf{r}')$ for (17), which satisfies

$$\begin{cases} -D_0 \Delta G_\omega + \alpha(\omega) G_\omega = \delta(\mathbf{r} - \mathbf{r}'), & x \in \Omega, \\ -D_0 \frac{\partial}{\partial z} G_\omega + \frac{1}{\zeta} G_\omega = 0, & x \in \partial\Omega. \end{cases} \quad (19)$$

We obtain

$$G_\omega(\mathbf{r}, \mathbf{r}') = \frac{1}{(2\pi)^2} \int_{\mathbb{R}^2} e^{i\mathbf{q} \cdot (\boldsymbol{\rho} - \boldsymbol{\rho}')} \tilde{G}_\omega(|\mathbf{q}|, z, z') d\mathbf{q}, \quad (20)$$

where

$$Q_\omega(q) = \sqrt{\frac{\alpha(\omega)}{D_0} + q^2}, \quad (21)$$

and

$$\tilde{G}_\omega(q, z, z') = \frac{1}{2D_0Q_\omega(q)} \left[e^{-Q_\omega(q)|z-z'|} - \frac{1 - Q_\omega(q)z_e}{1 + Q_\omega(q)z_e} e^{-Q_\omega(q)|z+z'|} \right] \quad (22)$$

for $q \in \mathbb{R}$.

Let v_0^n be the solution of the diffusion equation in (17) for which $\delta\mu_a$ is removed. We have

$$\begin{aligned} v_0^n(\mathbf{r}, \omega) &= f_0 \sum_{j=-\infty}^{\infty} \int_{-\infty}^{\infty} G_\omega \left(\mathbf{r}; jL + \frac{2n-1}{2}\ell, y', 0 \right) dy' \\ &= \frac{f_0}{L} \sum_{l=-\infty}^{\infty} \tilde{G}_\omega(p_l, z, 0) e^{ip_l x} e^{-ip_l(2n-1)\ell/2} \\ &= v_0^n(x, z, \omega), \end{aligned} \quad (23)$$

where the Green's function was expressed as $G_\omega(\mathbf{r}, \mathbf{r}') = G_\omega(\mathbf{r}; x', y', z')$.

We give detection points as

$$x_i = (i-1)h_d + x_{\text{init}} \quad (i = 1, \dots, N_d). \quad (24)$$

We will set

$$N_d = 33, \quad h_d = 2 \text{ mm}, \quad x_{\text{init}} = -32 \text{ mm}. \quad (25)$$

That is, $-32 \text{ mm} \leq x_i \leq 32 \text{ mm}$. We write $\mathbf{r}_d^{(i)} = {}^t(x_i, 0, 0)$. Within the diffusion approximation, we have

$$\ln \frac{v_0^n(\mathbf{r}_d^{(i)}, \omega)}{v^n(\mathbf{r}_d^{(i)}, \omega)} \approx \ln \frac{I_0^n(\mathbf{r}_d^{(i)}, -\hat{\mathbf{z}}, \omega)}{I^n(\mathbf{r}_d^{(i)}, -\hat{\mathbf{z}}, \omega)}, \quad (26)$$

where $\hat{\mathbf{z}} = {}^t(0, 0, 1)$. Here, $I_0^n(\mathbf{r}_d^{(i)}, -\hat{\mathbf{z}}, \omega)$ and $I^n(\mathbf{r}_d^{(i)}, -\hat{\mathbf{z}}, \omega)$ are Fourier transforms of specific intensities in the outer normal direction at $\mathbf{r}_d^{(i)}$ for $\mu_a = \bar{\mu}_a$ and $\mu_a = \bar{\mu}_a + \delta\mu_a$ with the n th scan.

We note that

$$\begin{aligned} &\int_{-\infty}^{\infty} G_\omega(\mathbf{r}, \mathbf{r}') dy' \\ &= \frac{1}{2\pi} \int_{-\infty}^{\infty} e^{iq(x-x')} \frac{1}{2D_0Q_\omega(q)} \\ &\quad \times \left[e^{-Q_\omega(q)|z-z'|} - \frac{1 - Q_\omega(q)z_e}{1 + Q_\omega(q)z_e} e^{-Q_\omega(q)|z+z'|} \right] dq \\ &= \frac{1}{\pi} \int_0^{\infty} \cos[q(x-x')] \frac{1}{2D_0Q_\omega(q)} \\ &\quad \times \left[e^{-Q_\omega(q)|z-z'|} - \frac{1 - Q_\omega(q)z_e}{1 + Q_\omega(q)z_e} e^{-Q_\omega(q)|z+z'|} \right] dq \\ &= H_\omega(x - x', z, z'). \end{aligned} \quad (27)$$

The numerical computation of H_ω is described in Appendix 4.

For each n , light is detected at N_d points. We define

$$\begin{aligned} \psi^n(x_i, \omega) &= v_0^n(x_i, 0, 0, \omega) \ln \frac{\langle I_0^n(\mathbf{r}_d^{(i)}, -\hat{\mathbf{z}}, \omega) \rangle}{\langle I^n(\mathbf{r}_d^{(i)}, -\hat{\mathbf{z}}, \omega) \rangle}, \\ & \quad i = 1, \dots, N_d, \end{aligned} \quad (28)$$

where $\langle \cdot \rangle$ denotes the average over y .

Since $\delta\mu_a$ does not depend on y , we write

$$\delta\mu_a(\mathbf{r}) = \eta(x, z). \quad (29)$$

We note the identity:

$$v^n(\mathbf{r}, \omega) = v_0^n(\mathbf{r}, \omega) - \int_{\Omega} G_\omega(\mathbf{r}, \mathbf{r}') \delta\mu_a(\mathbf{r}') v^n(\mathbf{r}', \omega) d\mathbf{r}'. \quad (30)$$

Since v_0^n is independent of y , the above identity implies $v^n(\mathbf{r}, \omega) = v^n(x, z, \omega)$ is also independent of y . We have

$$\begin{aligned} v^n(x, z, \omega) &= v_0^n(x, z, \omega) - \int_0^{\infty} \int_{-\infty}^{\infty} H_\omega(x - x', z, z') \\ &\quad \times \eta(x', z') v^n(x', z', \omega) dx' dz'. \end{aligned} \quad (31)$$

By the (first) Born approximation,

$$v^n \approx v_0^n + v_1^n, \quad (32)$$

where

$$\begin{aligned} v_1^n(x, z, \omega) &= - \int_0^{\infty} \int_{-\infty}^{\infty} v_0^n(x', z', \omega) H_\omega(x - x', z, z') \\ &\quad \times \eta(x', z') dx' dz'. \end{aligned} \quad (33)$$

Let us write

$$(K\eta)(x, \omega) = - \sum_{n=1}^{N_f} v_1^n(x, 0, \omega). \quad (34)$$

We have in the (first) Rytov approximation:

$$\sum_{n=1}^{N_f} \psi^n(x_i, \omega) = (K\eta)(x_i, \omega), \quad i = 1, \dots, N_d. \quad (35)$$

By the Fourier transform and summing over n , we introduce

$$\begin{aligned} \Psi(q, \omega) &= \sum_{n=1}^{N_f} \int_{-\infty}^{\infty} e^{-iqx} \psi^n(x, \omega) dx \\ &\approx \sum_{n=1}^{N_f} \int_{x_1}^{x_{N_d}} e^{-iqx} \psi^n(x, \omega) dx. \end{aligned} \quad (36)$$

Similarly we can introduce

$$(\tilde{K}\eta)(q, \omega) = \int_{-\infty}^{\infty} e^{-iqx} (K\eta)(x, \omega) dx. \quad (37)$$

We have

$$\begin{aligned} & (\tilde{K}\eta)(q, \omega) \\ &= \sum_{n=1}^{N_f} \int_{-\infty}^{\infty} e^{-iqx} \int_0^{\infty} \int_{-\infty}^{\infty} v_0^n(x', z', \omega) \\ & \quad \times H_{\omega}(x - x', 0, z') \eta(x', z') dx' dz' dx \\ &\approx \frac{1}{2} \sum_{n=1}^{N_f} \int_0^{\infty} \int_{-\infty}^{\infty} e^{-iqx'} \frac{v_0^n(x', z', \omega)}{D_0 Q_{\omega}(q_d)} \\ & \quad \times \left[e^{-Q_{\omega}(q)z'} - \frac{1 - Q_{\omega}(q)z_e}{1 + Q_{\omega}(q)z_e} e^{-Q_{\omega}(q)z'} \right] \\ & \quad \times \eta(x', z') dx' dz' \\ &= \frac{f_0}{L} \sum_{n=1}^{N_f} \sum_{l=-\infty}^{\infty} \int_0^{\infty} \tilde{G}_{\omega}(p_l, z', 0) e^{-ip_l(2n-1)\ell/2} \\ & \quad \times \tilde{G}_{\omega}(q, 0, z') \tilde{\eta}(q - p_l, z') dz', \end{aligned} \quad (38)$$

where we defined

$$\tilde{\eta}(q, z) = \int_{-\infty}^{\infty} e^{-iqx} \eta(x, z) dx. \quad (39)$$

Recalling $L = N_f \ell$, we can further proceed as

$$\begin{aligned} & (\tilde{K}\eta)(q, \omega) \\ &= \frac{f_0 N_f}{L} \sum_{l=mN_f, m \in \mathbb{Z}} \int_0^{\infty} e^{ip_l \ell/2} \tilde{G}_{\omega}(p_l, z', 0) \\ & \quad \times \tilde{G}_{\omega}(q, 0, z') \tilde{\eta}(q - p_l, z') dz' \\ &= \frac{f_0 N_f}{L} \sum_{m=-\infty}^{\infty} \int_0^{\infty} e^{i\pi m} \tilde{G}_{\omega}\left(\frac{2\pi m}{\ell}, z', 0\right) \\ & \quad \times \tilde{G}_{\omega}(q, 0, z') \tilde{\eta}\left(q - \frac{2\pi m}{\ell}, z'\right) dz' \\ &\approx \frac{f_0 N_f}{L} \int_0^{\infty} \tilde{G}_{\omega}(0, z', 0) \tilde{G}_{\omega}(q, 0, z') \tilde{\eta}(q, z') dz'. \end{aligned} \quad (40)$$

The formula for \tilde{G}_{ω} in (22) implies that $\tilde{G}_{\omega}(q, z', 0) < \tilde{G}_{\omega}(0, z', 0)$ for $q > 0, z' > 0$. Thus we arrive at the following linear problem:

$$\Psi(q, \omega) = \int_0^{\infty} \left[\frac{f_0 N_f}{h_d L} \tilde{G}_{\omega}(0, z', 0) \tilde{G}_{\omega}(q, 0, z') \right] \times \tilde{\eta}(q, z') dz'. \quad (41)$$

We can discretize ω, z as

$$\begin{aligned} \omega_k &= (k-1)\Delta\omega \quad (k=1, \dots, N_{\omega}), \\ \Delta\omega &= \frac{\omega_{\max}}{N_{\omega}-1}, \\ z_j &= (j-1)\Delta z + z_{\min} \quad (j=1, \dots, N_z), \\ \Delta z &= \frac{z_{\max} - z_{\min}}{N_z - 1}. \end{aligned} \quad (42)$$

Here,

$$\begin{aligned} N_{\omega} &= 100, \quad \omega_{\max} = 0.99 \text{ ps}^{-1}, \quad N_z = 80, \\ z_{\max} &= 40 \text{ mm}, \quad z_{\min} = 0.5 \text{ mm}. \end{aligned} \quad (44)$$

For each q , we solve the linear inverse problem which is given by

$$\mathbf{y}(q) = M(q)\mathbf{x}(q), \quad (45)$$

where $\mathbf{y}(q) \in \mathbb{C}^{N_{\omega}}$, $\mathbf{x}(q) \in \mathbb{C}^{N_z}$, $M(q) \in \mathbb{R}^{N_{\omega} \times N_z}$ are defined as

$$\{\mathbf{y}(q)\}_k = \Psi(q, \omega_k), \quad \{\mathbf{x}(q)\}_j = \tilde{\eta}(q, z_j), \quad (46)$$

and

$$\{M(q)\}_{kj} = \frac{f_0 \Delta z}{\ell^2} \tilde{G}_{\omega_k}(0, z_j, 0) \tilde{G}_{\omega_k}(q, 0, z_j). \quad (47)$$

Each inverse problem is solved as (see Appendix 5)

$$\mathbf{x}(q) \approx M_{\text{reg}}^+(q)\mathbf{y}(q), \quad (48)$$

where $M_{\text{reg}}^+(q)$ is the regularized pseudoinverse of $M(q)$. Let us discretize q as

$$q^{(k)} = \frac{2\pi}{h_d(2N_q+1)} k \quad (k = -N_q, \dots, N_q) \quad (49)$$

with

$$N_q = 16. \quad (50)$$

The truncated singular value decomposition was used to construct $M_{\text{reg}}^+(q^{(k)})$ with the threshold $\sigma_0 = 10^{-4}$ (see Appendix 5). As a result, two to four largest singular values were taken for each $q^{(k)}$.

Finally,

$$\eta(x_i, z_j) = \frac{1}{h_d(2N_q+1)} \sum_{k=-N_q}^{N_q} e^{iq^{(k)}x_i} \{\mathbf{x}(q^{(k)})\}_j, \quad i = 1, \dots, N_d, \quad j = 1, \dots, N_z. \quad (51)$$

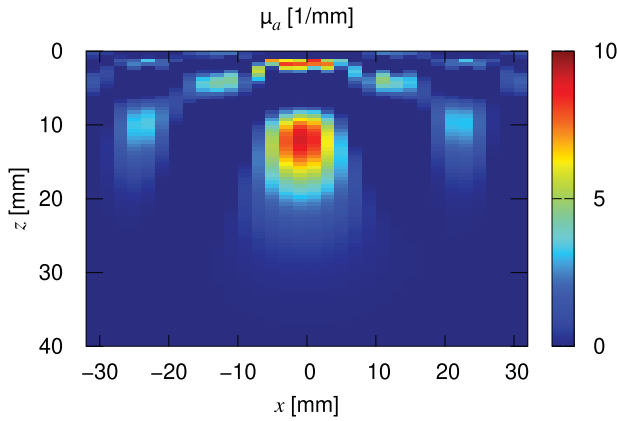


Figure 2. The reconstructed μ_a in (52). In the x - z plane, true positions of four corners of the absorber rectangle are $(-6, 4)$, $(-6, 10)$, $(0, 4)$ and $(0, 10)$ in the unit of mm.

4. Results

The reconstructed $\mu_a(\mathbf{r})$ is obtained as

$$\mu_a(x_i, z_j) \approx \bar{\mu}_a + \eta(x_i, z_j). \quad (52)$$

The result is plotted in Figure 2.

In Figure 3, the reconstruction was done for $L = 16$ mm ($N_f = 8$, $\sigma_0 = 10^{-4}$) and $L = 8$ mm ($N_f = 4$, $\sigma_0 = 10^{-2}$), respectively. The signal is weak and the reconstruction is vague when $L = 16$ mm. For $L = 8$ mm, the depth of the light propagation of the detected light is too shallow and the bar is not reconstructed. This behaviour can be understood from the depth of the banana which is discussed in Section 2 and Appendix 1.

5. Discussion

In this paper, the time-resolved measurement for the stripe illumination was proposed. The diffuse optical tomography was tested by using the forward data from Monte Carlo simulation. The time-dependent measurement which is considered in this paper can be realized by single-photon avalanche diode (SPAD) arrays [24].

In Figure 2, the x coordinate and size of the bar are reconstructed correctly. The z coordinate of the bar is reconstructed at a position deeper than the actual depth of the bar. The reconstructed value of μ_a is overestimated. There are numerous reasons for the depth and value of the reconstructed absorption bar. The bright part of the stripe illumination was modelled by the Dirac delta function as shown in (6), which does not have a width. The nonlinear inverse problem was linearized when tomographic images were computed. Indeed, the reconstruction was done in the transport regime, in which light propagation is governed by the radiative transport

equation. Moreover, only the constant mode $m = 0$ was taken into account for the operator \tilde{K} in (40).

Noisy reconstruction in Figure 2 near the boundary is commonly known [25]. A method to remove such high-frequency noise near the boundary was proposed [26].

Our optical tomography used all detected photons. Hence the reconstructions in Figure 3 are not good, which agree with the theory in Appendix 1. The situation might be different if selected photons are used; for example, Torricelli et al. proposed a novel approach of the null source-detector separation with late photons in time-resolved measurements [27].

Since the proposed optical tomography uses time-resolved data, a natural next step is the reconstruction of both the absorption and reduced scattering coefficients. The reconstruction of two parameters by the Rytov approximation [28] will be utilized for the stripe illumination.

The penetration depth of near-infrared light can be controlled with the pitch L of the stripe. Although this fact is empirically well known, we studied the situation in Appendix 1 by obtaining the depth of the banana shape. In [29], $\langle z \rangle_{d_{SD}}$ (see Section 2) was considered for a specific refractive-index ratio $\zeta = 5.91$, which corresponds to $n \approx 1.36$. In Appendix 1, the banana depth z_0 is derived for general n . Although the formula (A26) was established from numerical experiments, z_0 in (A18) is derived from diffusion theory. We should emphasize that z_0 is introduced as the depth at which the point absorber most affects the detected light whereas the empirical relation $\langle z \rangle_{d_{SD}}$ is the average depth. Hence, z_0 and $\langle z \rangle_{d_{SD}}$ do not necessarily coincide even for $n = 1.36$.

As shown in Appendix 1, a simple formula of $z_0 = d_{SD}/(2\sqrt{2})$ was obtained when the absorption is negligible for the zero boundary condition, where d_{SD} is the source-detector distance. The same formula was derived with a different way in the banana-shape regions theory [14]. In this paper, the formula z_0 is calculated for general cases. We note that the paths of detected photons exist a lot deeper places although we focused on the depth of the banana in this paper. The theory and simulation in [30] show that the average of the maximum penetration depth is deeper than z_0 .

To discuss the typical penetration depth, let us consider the separation L between the two stripes since the outgoing light at multiple pitches away is negligible. Although the distance of interest is the pitch of stripes instead of the separation between two points, if we set d_{SD} as $d_{SD} = (L - \ell)/2 = 15$ mm ($L = 32$ mm, $\ell = 2$ mm), the formula in Appendix 1 implies that the information at a deep tissue can be extracted with large L . Let us estimate the most probable depth of detected photons

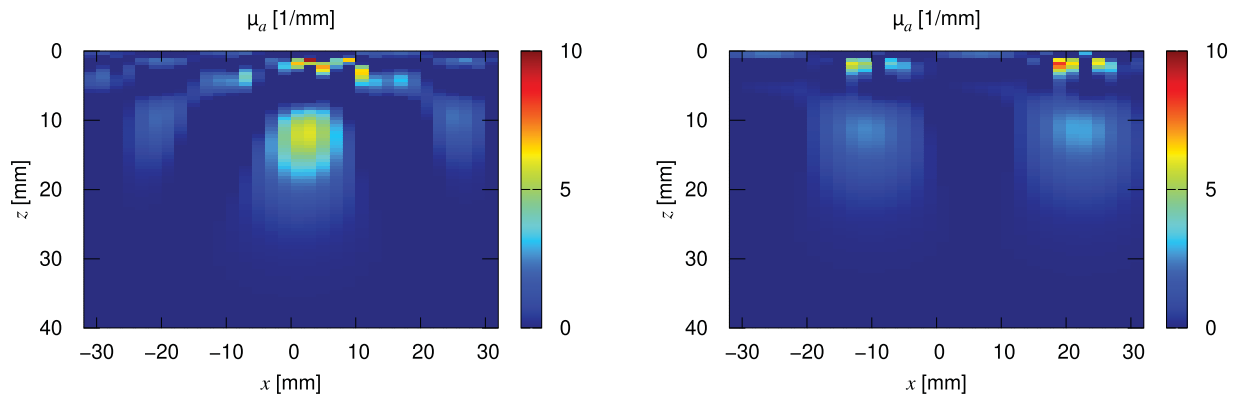


Figure 3. The reconstructed μ_a in (52) for (left) $L = 16$ mm and (right) $L = 8$ mm. In the x - z plane, true positions of four corners of the absorber rectangle are $(-6, 4)$, $(-6, 10)$, $(0, 4)$ and $(0, 10)$ in the unit of mm.

using the calculation in Appendix 1 although light was illuminated along a stripe in the optical tomography. Assuming the relation $z_0 \approx 0.2d_{SD}$, we find that the most probable depth is about 3 mm. The depth of the target is slightly deeper than 3 mm.

Disclosure statement

No potential conflict of interest was reported by the author(s).

Funding

This work was supported by JST, CREST Grant Number JPMJCR22C1, Japan. MM acknowledges support from JSPS KAKENHI Grant No. JP18K03438 and JST PRESTO Grant No. JPMJPR2027. KK acknowledges support from JSPS KAKENHI Grant Nos. JP16K04985, JP17H06102, JP18H01497, JP18H05240. The Monte Carlo eXtreme (MCX) (<http://mcx.space/>) was used for Monte Carlo simulation. We truly thank Eiji Okada for providing Monte Carlo data for the banana-shape calculation in Appendices 1 and 2.

References

- [1] Boas DA, Elwell CE, Ferrari M, et al. Twenty years of functional near-infrared spectroscopy: introduction for the special issue. *NeuroImage*. **2014**;85:1–5. doi: [10.1016/j.neuroimage.2013.11.033](https://doi.org/10.1016/j.neuroimage.2013.11.033)
- [2] Eggebrecht AT, Ferradal SL, Robichaux-Viehoever A, et al. Mapping distributed brain function and networks with diffuse optical tomography. *Nat Photonics*. **2014**;8:448–454. doi: [10.1038/nphoton.2014.107](https://doi.org/10.1038/nphoton.2014.107)
- [3] Mazurenka M, Di Sieno L, Boso G, et al. Non-contact in vivo diffuse optical imaging using a time-gated scanning system. *Biomed Opt Express*. **2013**;4:2257–2268. doi: [10.1364/BOE.4.002257](https://doi.org/10.1364/BOE.4.002257)
- [4] Machida M, Panasyuk GY, Wang Z-M, et al. Radiative transport and optical tomography with large datasets. *J Opt Soc Am A*. **2016**;33:551–558. doi: [10.1364/JOSAA.33.000551](https://doi.org/10.1364/JOSAA.33.000551)
- [5] Cuccia DJ, Bevilacqua F, Durkin AJ, et al. Modulated imaging: quantitative analysis and tomography of turbid media in the spatial-frequency domain. *Opt Lett*. **2005**;30:1354–1356. doi: [10.1364/OL.30.001354](https://doi.org/10.1364/OL.30.001354)
- [6] Cuccia DJ, Bevilacqua F, Durkin AJ, et al. Quantitation and mapping of tissue optical properties using modulated imaging. *J Biomed Opt*. **2009**;14:024012. doi: [10.1117/1.3088140](https://doi.org/10.1117/1.3088140)
- [7] Angelo JP, Chen S-J, Ochoa M, et al. Review of structured light in diffuse optical imaging. *J Biomed Opt*. **2019**;24:071602.
- [8] Bai W, Dong Y, Zhang Y, et al. Wide-field illumination diffuse optical tomography within a framework of single-pixel time-domain spatial frequency domain imaging. *Opt Express*. **2024**;32:6104–6120. doi: [10.1364/OE.513909](https://doi.org/10.1364/OE.513909)
- [9] Takada K, Osada K, Machida M, et al. Spatio-temporal frequency domain imaging using time-resolving CMOS image sensor and stripe pattern projection. In: *optical tomography and spectroscopy of tissue XIV* edited by S. Fantini, P. Taroni Proc SPIE 2021; Vol. 11639. p. 116391C.
- [10] Hock C, Villringer K, Müller-Spahn F, et al. Decrease in parietal cerebral hemoglobin oxygenation during performance of a verbal fluency task in patients with Alzheimer's disease monitored by means of near-infrared spectroscopy (NIRS)—correlation with simultaneous rCBF-PET measurements. *Brain Res*. **1997**;755:293–303. doi: [10.1016/S0006-8993\(97\)00122-4](https://doi.org/10.1016/S0006-8993(97)00122-4)
- [11] Quaresima V, Ferrari M. Functional near-infrared spectroscopy (fNIRS) for assessing cerebral cortex function during human behavior in natural/social situations: A concise review. *Org Res Meth*. **2019**;22:46–68. doi: [10.1177/1094428116658959](https://doi.org/10.1177/1094428116658959)
- [12] Weiss GH, Nossal R, Bonner RF. Statistics of penetration depth of photons re-emitted from irradiated tissue. *J Modern Opt*. **1989**;36:349–359. doi: [10.1080/09500348914550381](https://doi.org/10.1080/09500348914550381)
- [13] Schotland JC, Haselgrove JC, Leigh JS. Photon hitting density. *Appl Opt*. **1993**;32:448–453. doi: [10.1364/AO.32.000448](https://doi.org/10.1364/AO.32.000448)
- [14] Feng S, Zeng F-A, Chance B. Photon migration in the presence of a single defect: a perturbation analysis. *Appl Opt*. **1995**;34:3826–3837. doi: [10.1364/AO.34.003826](https://doi.org/10.1364/AO.34.003826)
- [15] Zhu XD, Wei S, Feng SC, et al. Analysis of a diffuse-photon-density wave in multiple-scattering media in the presence of a small spherical object. *J Opt Soc Am A*. **1996**;13:494–499. doi: [10.1364/JOSAA.13.000494](https://doi.org/10.1364/JOSAA.13.000494)
- [16] Boas DA, Brooks DH, Miller EL, et al. Imaging the body with diffuse optical tomography. *IEEE Signal Process Mag*. **2001**;18:57–75. doi: [10.1109/79.962278](https://doi.org/10.1109/79.962278)

- [17] Sassaroli A, Pifferi A, Contini D, et al. Forward solvers for photon migration in the presence of highly and totally absorbing objects embedded inside diffusive media. *J Opt Soc Am A*. **2014**;31:460–469. doi: [10.1364/JOSAA.31.00460](https://doi.org/10.1364/JOSAA.31.00460)
- [18] Ishimaru A. Wave propagation and scattering in random media. Vol. San Diego: Academic Press; 1978.
- [19] Egan WG, Hilgeman TW. Optical properties of inhomogeneous materials. New York: Academic Press; 1979.
- [20] Haskell RC, Svaasand LO, Tsay T-T, et al. Boundary conditions for the diffusion equation in radiative transfer. *J Opt Soc Am A*. **1994**;11:2727–2741. doi: [10.1364/JOSAA.11.002727](https://doi.org/10.1364/JOSAA.11.002727)
- [21] Contini D, Martelli F, Zaccanti G. Photon migration through a turbid slab described by a model based on diffusion approximation. I. Theory *Appl Opt*. **1997**;36:4587–4599. doi: [10.1364/AO.36.004587](https://doi.org/10.1364/AO.36.004587)
- [22] Machida M, Hoshi Y, Kagawa K, et al. Decay behavior and optical parameter identification for spatial-frequency domain imaging by the radiative transport equation. *J Opt Soc Am A*. **2020**;37:2020–2031. doi: [10.1364/JOSAA.402124](https://doi.org/10.1364/JOSAA.402124)
- [23] Fang Q, Boas D. Monte Carlo simulation of photon migration in 3D turbid media accelerated by graphics processing units. *Opt Express*. **2009**;17:20178–20190. doi: [10.1364/OE.17.020178](https://doi.org/10.1364/OE.17.020178)
- [24] Bruschini C, Homulle H, Antolovic IM, et al. Single-photon avalanche diode imagers in biophotonics: review and outlook. *Light Sci Appl*. **2019**;8:87. doi: [10.1038/s41377-019-0191-5](https://doi.org/10.1038/s41377-019-0191-5)
- [25] Hebden JC, Schmidt FEW, Fry ME, et al. Simultaneous reconstruction of absorption and scattering images by multichannel measurement of purely temporal data. *Opt Lett*. **1999**;24:534–536. doi: [10.1364/OL.24.000534](https://doi.org/10.1364/OL.24.000534)
- [26] Srinivasan S, Pogue BW, Dehghani H, et al. Improved quantification of small objects in near-infrared diffuse optical tomography. *J Biomed Opt*. **2004**;9:1161–1171. doi: [10.1117/1.1803545](https://doi.org/10.1117/1.1803545)
- [27] Torricelli A, Pifferi A, Spinelli L, et al. Time-resolved reflectance at null source-detector separation: improving contrast and resolution in diffuse optical imaging. *Phys Rev Lett*. **2005**;95:078101. doi: [10.1103/PhysRevLett.95.078101](https://doi.org/10.1103/PhysRevLett.95.078101)
- [28] Markel VA, Schotland JC. Symmetries, inversion formulas, and image reconstruction for optical tomography. *Phys Rev E*. **2004**;70:056616. doi: [10.1103/PhysRevE.70.056616](https://doi.org/10.1103/PhysRevE.70.056616)
- [29] Patterson MS, Andersson-Engels S, Wilson BC, et al. Absorption spectroscopy in tissue-simulating materials: a theoretical and experimental study of photon paths. *Appl Opt*. **1995**;34:22–30. doi: [10.1364/AO.34.000022](https://doi.org/10.1364/AO.34.000022)
- [30] Martelli F, Binzoni T, Pifferi A, et al. There's plenty of light at the bottom: statistics of photon penetration depth in random media. *Sci Reports*. **2016**;6:27057.
- [31] Arridge SR. Optical tomography in medical imaging. *Inverse Probl*. **1999**;15:R41–R93. doi: [10.1088/0266-5611/15/2/022](https://doi.org/10.1088/0266-5611/15/2/022)
- [32] Roach GF. Green's functions: introductory theory with applications. London: Van Nostrand Reinhold Company; 1970.
- [33] Kraut EA. Fundamentals of mathematical physics. New York: Dover Publications; 2007.
- [34] Jacques SL. Optical properties of biological tissues: a review. *Phys Med Biol*. **2013**;58:R37–R61. doi: [10.1088/0031-9155/58/11/R37](https://doi.org/10.1088/0031-9155/58/11/R37)
- [35] Arridge SR. Photon-measurement density functions. Part I: analytical forms. *Appl Opt*. **1995**;34:7395–7409. doi: [10.1364/AO.34.007395](https://doi.org/10.1364/AO.34.007395)
- [36] Arridge SR, Schweiger M. Photon-measurement density functions. Part 2: finite-element-method calculations. *Appl Opt*. **1995**;34:8026–8037. doi: [10.1364/AO.34.008026](https://doi.org/10.1364/AO.34.008026)
- [37] Okada E, Delpy DT. Near-infrared light propagation in an adult head model. I. Modeling of low-level scattering in the cerebrospinal fluid layer. *Appl Opt*. **2003**;42:2906–2914. doi: [10.1364/AO.42.002906](https://doi.org/10.1364/AO.42.002906)
- [38] Ooura T, Mori M. The double exponential formula for oscillatory functions over the half infinite interval. *J Comput Appl Math*. **1991**;38:353–360. doi: [10.1016/0377-0427\(91\)90181-1](https://doi.org/10.1016/0377-0427(91)90181-1)
- [39] Ooura T, Mori M. A robust double exponential formula for Fourier-type integrals. *J Comput Appl Math*. **1999**;112:229–241. doi: [10.1016/S0377-0427\(99\)00223-X](https://doi.org/10.1016/S0377-0427(99)00223-X)
- [40] Ogata H. A numerical integration formula based on the Bessel functions. *Publ RIMS Kyoto Univ*. **2005**;41:949–970. doi: [10.4171/prims](https://doi.org/10.4171/prims)

Appendix 1. Banana shape

To give insight about the penetration depth of detected photons for the stripe illumination, we here consider the light propagation from one point to another on the surface ($\partial\Omega$) of the medium. Moreover, since the optical tomography is considered using all detected photons in Section 3, we analyse the time-independent diffusion equation.

Suppose that light is illuminated at $\mathbf{r}_s \in \partial\Omega$ and detected at another point $\mathbf{r}_d \in \partial\Omega$. Let $\mathbf{r}_s = {}^t(x_s, 0, 0^+)$ and $\mathbf{r}_d = {}^t(x_d, 0, 0)$ with $-x_s = x_d = d_{SD}/2 > 0$, i.e. d_{SD} is the distance between the source and detector (Figure A1). Let $u(\mathbf{r}; \mathbf{r}_s)$ be the diffuse fluence rate at \mathbf{r} . The light propagation is governed by the following diffusion equation [18]:

$$\begin{cases} -D_0 \Delta u + \bar{\mu}_a u = \delta(\mathbf{r} - \mathbf{r}_s), & \mathbf{r} \in \Omega, \\ -D_0 \frac{\partial}{\partial z} u + \frac{1}{\zeta} u = 0, & \mathbf{r} \in \partial\Omega. \end{cases} \quad (\text{A1})$$

We note that (2) reduces to (A1) by the integration over t and setting $\delta\mu_a = 0, f(\mathbf{r}, t) = \delta(\mathbf{r} - \mathbf{r}_s)\delta(t)$.

To investigate the propagation of the detected light, we suppose that there is a point absorber at $\mathbf{r}_0 = {}^t(x_0, 0, z_0)$ and consider the diffusion equation for $U(\mathbf{r}; \mathbf{r}_0, \mathbf{r}_s)$ which is given by

$$\begin{cases} -D_0 \Delta U + \mu_a(\mathbf{r})U = \delta(\mathbf{r} - \mathbf{r}_s), & \mathbf{r} \in \Omega, \\ -D_0 \frac{\partial}{\partial z} U + \frac{1}{\zeta} U = 0, & \mathbf{r} \in \partial\Omega. \end{cases} \quad (\text{A2})$$

Here,

$$\mu_a(\mathbf{r}) = \bar{\mu}_a + \eta_0 \delta(\mathbf{r} - \mathbf{r}_0), \quad (\text{A3})$$

where $\eta_0 > 0$ is a constant. The idea to detect the shape of the banana is similar to the idea used in the banana-shape regions theory [14,15,17] in the sense that an absorber is assumed. However, we assume a point absorber instead of a sphere and will consider the depth of the banana instead of its shape. We

IMPULSE STRIPE ILLUMINATION

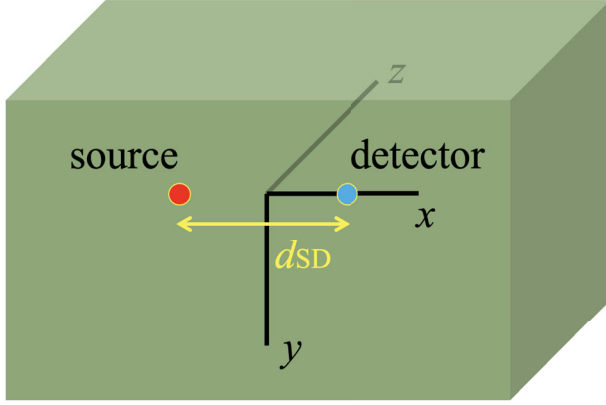


Figure A1. Schematic figure (top view). Light is illuminated at $(-d_{SD}/2, 0, 0)$ (red circle) and detected at $(d_{SD}/2, 0, 0)$ (blue circle) on the boundary of the half space.

assume that η_0 is small so that the Born approximation (below) holds.

By subtracting (A1) from (A2), we have

$$\begin{cases} -D_0 \Delta(U - u) + \bar{\mu}_a(U - u) = S, & \mathbf{r} \in \Omega, \\ -D_0 \frac{\partial}{\partial z}(U - u) + \frac{1}{\zeta}(U - u) = 0, & \mathbf{r} \in \partial\Omega, \end{cases} \quad (\text{A4})$$

where

$$S(\mathbf{r}; \mathbf{r}_0, \mathbf{r}_s) = -\eta_0 \delta(\mathbf{r} - \mathbf{r}_0) U(\mathbf{r}; \mathbf{r}_0, \mathbf{r}_s). \quad (\text{A5})$$

From (A4), we obtain

$$U(\mathbf{r}; \mathbf{r}_0, \mathbf{r}_s) - u(\mathbf{r}; \mathbf{r}_s) = \int_{\Omega} G(\mathbf{r}, \mathbf{r}') S(\mathbf{r}'; \mathbf{r}_0, \mathbf{r}_s) d\mathbf{r}', \quad (\text{A6})$$

where the Green's function $G(\mathbf{r}, \mathbf{r}')$ was introduced as

$$\begin{cases} -D_0 \Delta G + \bar{\mu}_a G = \delta(\mathbf{r} - \mathbf{r}'), & \mathbf{r} \in \Omega, \\ -D_0 \frac{\partial}{\partial z} G + \frac{1}{\zeta} G = 0, & \mathbf{r} \in \partial\Omega. \end{cases} \quad (\text{A7})$$

We note that $u(\mathbf{r}; \mathbf{r}_s) = G(\mathbf{r}, \mathbf{r}_s)$. Thus the following identity is derived.

$$U(\mathbf{r}; \mathbf{r}_0, \mathbf{r}_s) = G(\mathbf{r}, \mathbf{r}_s) - \eta_0 G(\mathbf{r}, \mathbf{r}_0) U(\mathbf{r}_0; \mathbf{r}_0, \mathbf{r}_s) \quad (\text{A8})$$

With the Born approximation [31], we have $U(\mathbf{r}; \mathbf{r}_0, \mathbf{r}_s) \approx u_B(\mathbf{r}_s, \mathbf{r}_0, \mathbf{r})$, where

$$u_B(\mathbf{r}_s, \mathbf{r}_0, \mathbf{r}) = G(\mathbf{r}, \mathbf{r}_s) - \eta_0 G(\mathbf{r}, \mathbf{r}_0) G(\mathbf{r}_0, \mathbf{r}_s). \quad (\text{A9})$$

Let $J_0(\cdot)$ be the Bessel function of the first kind of order zero. We have (see Appendix 3)

$$\begin{aligned} G(\mathbf{r}_0, \mathbf{r}_s) &= \frac{z_e}{2\pi D_0} \int_0^\infty q J_0(q|x_0 - x_s|) \frac{e^{-\lambda(q)z_0}}{1 + \lambda(q)z_e} dq, \\ G(\mathbf{r}_0, \mathbf{r}_d) &= \frac{z_e}{2\pi D_0} \int_0^\infty q J_0(q|x_0 - x_d|) \frac{e^{-\lambda(q)z_0}}{1 + \lambda(q)z_e} dq, \end{aligned} \quad (\text{A10})$$

where

$$\lambda(q) = \sqrt{\frac{\bar{\mu}_a}{D_0} + q^2}, \quad z_e = \zeta D_0. \quad (\text{A11})$$

Here, $q \geq 0$ is the magnitude of the Fourier vector \mathbf{q} (see (A27)). We note the reciprocal property $G(\mathbf{r}, \mathbf{r}') = G(\mathbf{r}', \mathbf{r})$ [32,33].

Since

$$\begin{aligned} \frac{\partial}{\partial z_0} u_B(\mathbf{r}_s, \mathbf{r}_0, \mathbf{r}_d) &= -\eta_0 \left[\frac{\partial G(\mathbf{r}_d, \mathbf{r}_0)}{\partial z_0} G(\mathbf{r}_0, \mathbf{r}_s) \right. \\ &\quad \left. + G(\mathbf{r}_d, \mathbf{r}_0) \frac{\partial G(\mathbf{r}_0, \mathbf{r}_s)}{\partial z_0} \right], \end{aligned} \quad (\text{A12})$$

we obtain

$$\begin{aligned} \frac{\partial}{\partial z_0} u_B(\mathbf{r}_s, \mathbf{r}_0, \mathbf{r}_d) &= \eta_0 \left(\frac{z_e}{2\pi D_0} \right)^2 \\ &\times \left[\left(\int_0^\infty q J_0(q|x_0 - x_d|) \frac{\lambda(q) e^{-\lambda(q)z_0}}{1 + \lambda(q)z_e} dq \right) \right. \\ &\times \left(\int_0^\infty q J_0(q|x_0 - x_s|) \frac{e^{-\lambda(q)z_0}}{1 + \lambda(q)z_e} dq \right) \\ &+ \left(\int_0^\infty q J_0(q|x_0 - x_d|) \frac{e^{-\lambda(q)z_0}}{1 + \lambda(q)z_e} dq \right) \\ &\times \left. \left(\int_0^\infty q J_0(q|x_0 - x_s|) \frac{\lambda(q) e^{-\lambda(q)z_0}}{1 + \lambda(q)z_e} dq \right) \right]. \end{aligned} \quad (\text{A13})$$

Let us investigate the position of the centre of the banana shape by moving the point absorber. Since photons that propagate through the banana are detected, the detected light is most affected if the point source is placed in the banana. In particular, the detected light must be affected most if the absorber is placed at the centre of the banana. Thus we can obtain the centre position of the banana by finding the minimum of the detected light $u(\mathbf{r}_d; \mathbf{r}_0, \mathbf{r}_s)$ when the position \mathbf{r}_0 of the absorber is moved. Since we assumed that η_0 is sufficiently small, we can solve this minimization problem by using u_B instead of u . Recall that the solution of (A1) is indeed the Green's function. The reciprocal property of the Green's function implies that the banana is symmetric about \mathbf{r}_s and \mathbf{r}_d . Hence, hereafter we set $x_0 = 0$. Now the position of the absorber is given by $\mathbf{r}_0 = {}^t(0, 0, z_0)$. The rest is to find z_0 which minimizes u_B .

If the point absorber is placed at the centre of the banana, we have $\frac{\partial}{\partial z_0} u_B(\mathbf{r}_s, \mathbf{r}_0, \mathbf{r}_d) = 0$. Using $|x_0 - x_d| = |x_0 - x_s| = d_{SD}/2$ in (A13), the condition of the zero derivative implies

$$\int_0^\infty q J_0\left(\frac{qd_{SD}}{2}\right) \frac{\lambda(q) e^{-\lambda(q)z_0}}{1 + \lambda(q)z_e} dq = 0. \quad (\text{A14})$$

By using $qdq = \lambda d\lambda$ and setting $x = \lambda d_{SD}/2$, we have

$$\begin{aligned} &\int_{\sqrt{\frac{\bar{\mu}_a}{D_0}}}^\infty J_0\left(\frac{d_{SD}}{2} \sqrt{\lambda^2 - \frac{\bar{\mu}_a}{D_0}}\right) \frac{\lambda^2 e^{-\lambda z_0}}{1 + \lambda z_e} d\lambda \\ &= \left(\frac{2}{d_{SD}}\right)^3 \int_a^\infty J_0(\sqrt{x^2 - a^2}) \frac{x^2 e^{-wx}}{1 + bx} dx = 0, \end{aligned} \quad (\text{A15})$$

where

$$a = \frac{d_{SD}}{2} \sqrt{\frac{\bar{\mu}_a}{D_0}}, \quad b = \frac{2z_e}{d_{SD}}, \quad w = \frac{2z_0}{d_{SD}}. \quad (\text{A16})$$

Thus the problem reduces to the problem of finding the zero of the following function $\Lambda(w)$:

$$\Lambda(w; a, b) = \int_a^\infty J_0(\sqrt{x^2 - a^2}) \frac{x^2 e^{-wx}}{1 + bx} dx. \quad (\text{A17})$$

Let $w_* = w_*(d_{\text{SD}}; \bar{\mu}_a, D_0, n)$ be the positive number such that $\Lambda(w_*; a, b) = 0$. In general, this w_* can be obtained numerically. Then the depth of the banana is obtained as

$$z_0 = \frac{d_{\text{SD}}}{2} w_*. \quad (\text{A18})$$

We note that $\Lambda(w; a, b)$ can be expressed as

$$\Lambda(w; a, b) = \int_0^\infty J_0(y) \frac{\sqrt{y^2 + a^2} e^{-w\sqrt{y^2 + a^2}}}{1 + b\sqrt{y^2 + a^2}} y dy, \quad (\text{A19})$$

where the variables were changed as $y = \sqrt{x^2 - a^2}$ ($x dx = y dy$).

The existence of the solution w_* can be relatively easily proved as follows if $\bar{\mu}_a$ is negligibly small. In this case, we can set $a = 0$. Then for large w ,

$$\begin{aligned} \Lambda(w; 0, b) &= \int_0^\infty J_0(x) \frac{x^2 e^{-wx}}{1 + bx} dx \\ &\approx \int_0^\infty x^2 e^{-wx} dx = \frac{2}{w^3} > 0. \end{aligned} \quad (\text{A20})$$

When $w = 0$, we have

$$\begin{aligned} \Lambda(0; 0, b) &= \int_0^\infty J_0(x) \frac{x^2}{1 + bx} dx \\ &= \frac{1}{b} \int_0^\infty J_0(x) x dx - \frac{1}{b} \int_0^\infty J_0(x) \frac{x}{1 + bx} dx \\ &= -\frac{1}{b^3} \int_0^\infty J_0(t/b) \frac{t}{1 + t} dt \\ &= -\frac{1}{b^2} + \frac{\pi}{2b^3} \left(H_0\left(\frac{1}{b}\right) - Y_0\left(\frac{1}{b}\right) \right) < 0, \end{aligned} \quad (\text{A21})$$

where we used the Hankel transform $\int_0^\infty J_0(qx) x dx = \delta(q)/q$. Here the Struve function H_0 and Bessel function of the second

kind Y_0 are given by

$$\begin{aligned} H_0(x) &= \frac{1}{\sqrt{\pi}} \sum_{n=0}^{\infty} \frac{(-1)^n x^{2n+1}}{[(2n+1)!!] 2^n \Gamma(n+3/2)}, \\ Y_0(x) &= \frac{1}{\pi} \left(\frac{\partial J_\nu(x)}{\partial \nu} - \frac{\partial J_{-\nu}(x)}{\partial \nu} \right) \Big|_{\nu=0} \\ &= \frac{2}{\pi} J_0(x) \ln \frac{x}{2} - \frac{2}{\pi} \sum_{n=0}^{\infty} \frac{(-1)^n}{(n!)^2} \left(\frac{x}{2} \right)^{2n} \psi(n+1), \end{aligned} \quad (\text{A22})$$

where ψ is the digamma function. The facts that $\Lambda(w; 0, b)$ is positive for large w and negative for small $w > 0$ imply that $\Lambda(w; 0, b)$ has a zero.

If in addition, $b = 0$ (i.e. the zero boundary condition $z_e = 0$), the depth z_0 is obtained explicitly; we obtain

$$\Lambda(w; 0, 0) = \int_0^\infty J_0(x) x^2 e^{-wx} dx = \frac{\sqrt{w^2 + 1} (2w^2 - 1)}{(1 + w^2)^3}. \quad (\text{A23})$$

Hence $w_* = 1/\sqrt{2}$. In the case that $\bar{\mu}_a$ is negligibly small and $z_e = 0$, the depth is given by $z_0 = d_{\text{SD}}/(2\sqrt{2}) \approx 0.35 d_{\text{SD}}$.

Let us find w_* for general cases by plotting (A17). To proceed, we assume physiological parameters [34]: $\bar{\mu}_a = 0.01 \text{ mm}^{-1}$ and $\mu'_s = 1 \text{ mm}^{-1}$. That is, $a \approx 0.0866 d_{\text{SD}}$. Hereafter in this section, the boundary condition is not restricted to the zero boundary condition.

To numerically handle the oscillatory integral in (A17), we changed the variable as $y = \sqrt{x^2 - a^2}$ and used the expression (A19). In Figures A2 and A3, $\Lambda(w; a, b)$ is plotted against w for different d_{SD} . The zero boundary condition ($z_e = 0$) was assumed in the left panel of Figure A2. In Figure A2 (Left), $w_* = 0.49$ for $d_{\text{SD}} = 30 \text{ mm}$. In the case of the zero boundary condition, the depth of the banana is estimated as $z_0 = 7.5 \text{ mm}$. The right panel of Figure A2 shows $\Lambda(w; a, b)$ in the case of $n = 1.4$. We found $w_* = 0.38$ for $d_{\text{SD}} = 30 \text{ mm}$ and $z_0 = 5.7 \text{ mm}$ in Figure A2 (Right). In Figure A3, (Left) $n = 1.33$ and (Right) $n = 1.37$. In both panels in Figure A3, $w_* = 0.39$ for $d_{\text{SD}} = 30 \text{ mm}$ and $z_0 = 5.9 \text{ mm}$. We found $w_* \approx 0.4$ for the Robin boundary condition in Figure A2 (Right), and Figure A3 (Left)

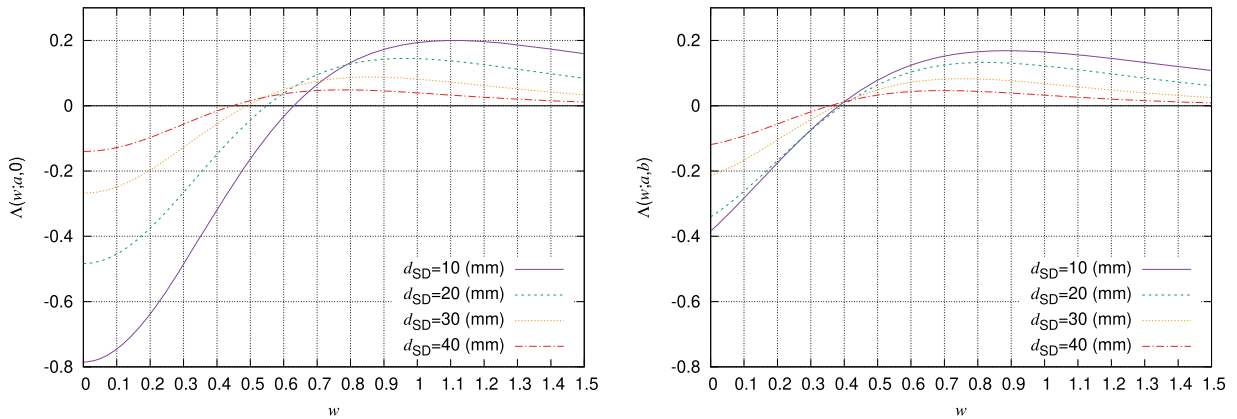


Figure A2. (Left) The function $\Lambda(w; a, 0)$ is plotted for different d_{SD} . (Right) The function $\Lambda(w; a, b)$ is plotted for different d_{SD} for $n = 1.4$.

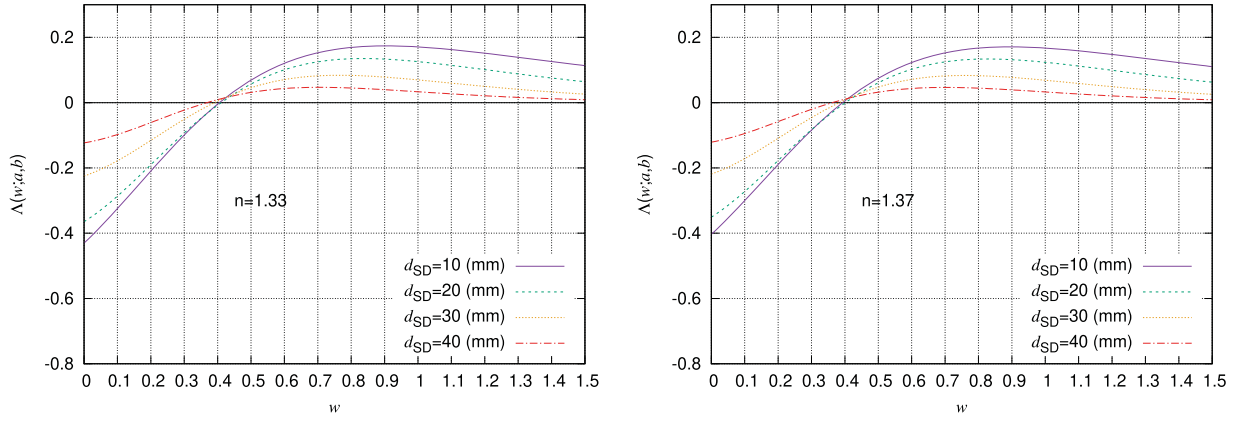


Figure A3. The function $\Lambda(w; a, b)$ is plotted for different d_{SD} for (Left) $n = 1.33$ and (Right) $n = 1.37$.

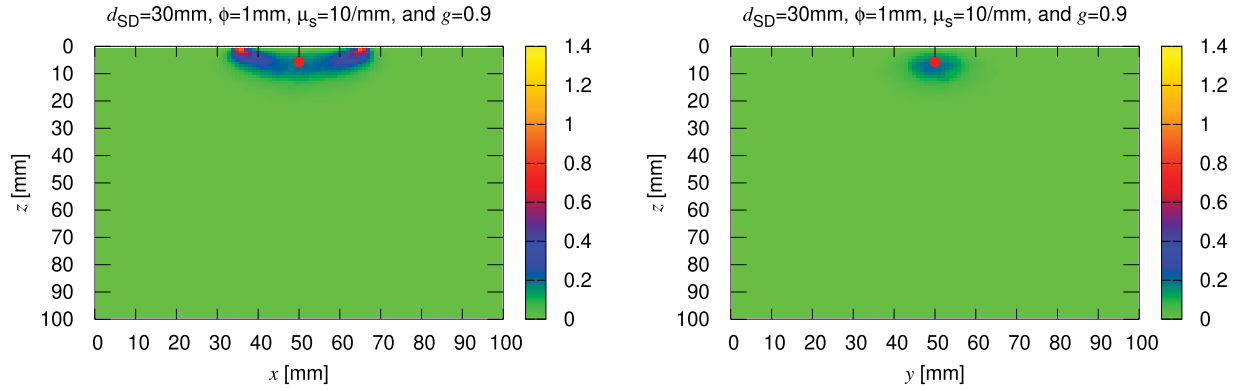


Figure A4. The spatial sensitivity profile is shown for $d_{SD} = 30$ mm, $\phi = 1$ mm, $\mu_s = 10$ mm $^{-1}$ and $g = 0.9$ ($\mu'_s = 1$ mm $^{-1}$). The cross sections at (Left) $y = 50$ mm and (Right) $x = 50$ mm are shown. The point at $z = z_0$ is shown by a solid red circle.

Table A1. The relation between d_{SD} and w_* is shown in four tables, from the left, for $z_e = 0$ (zero boundary condition) read from Figure A2 (Left), $n = 1.4$ read from Figure A2 (Right), $n = 1.33$ read from Figure A3 (Left), and $n = 1.37$ read from Figure A3 (Right).

$z_e = 0$		$n = 1.4$		$n = 1.33$		$n = 1.37$	
d_{SD} [mm]	w_*						
10	0.63	10	0.38	10	0.41	10	0.40
20	0.55	20	0.40	20	0.41	20	0.40
30	0.49	30	0.38	30	0.39	30	0.39
40	0.45	40	0.36	40	0.37	40	0.36

and (Right). That is, we have an approximate relation:

$$z_0 \approx 0.2d_{SD}. \quad (\text{A24})$$

Zeros w_* found in Figures A2 and A3 are summarized in Tables A1. Recalling that w_* is proportional to z_0 , we see that the banana is deeper for the zero boundary condition than the banana when light is reflected on the surface. For the zero boundary condition with $d_{SD} \approx 3$ cm, we have

$$z_0 \approx 0.25d_{SD}. \quad (\text{A25})$$

In Figures A4 and A5, we plot z_0 with the spatial sensitivity profile [35–37], which was obtained by Monte Carlo simulation. Let ϕ, g be the diameter of an optical fibre and scattering asymmetry parameter, respectively. The diameter ϕ is

set to 1 mm in Figures A4 and A5. We set $\bar{\mu}_a = 0.01$ mm $^{-1}$. We note $\mu'_s = (1 - g)\mu_s = 1$ mm $^{-1}$, where μ_s is the scattering coefficient. The source and detector were placed on the x -axis. In both Figures A4 and A5, planes at (Left) $y = 50$ mm and (Right) $x = 50$ mm are shown. The centre position of the banana at z_0 is shown by a solid red circle in both cases of $d_{SD} = 30$ mm and $d_{SD} = 40$ mm. In Monte Carlo simulation, the refractive index of the medium was set to $n = 1.4$ and the Fresnel reflection was assumed on the boundary.

More results from Monte Carlo simulation are shown in Appendix 2. Spatial sensitivity profiles are shown for (Figure A6) $d_{SD} = 30$ mm, $\phi = 1$ mm, $\mu_s = 1$ mm $^{-1}$, $g = 0.0$ ($\mu'_s = 1$ mm $^{-1}$), (Figure A7) $d_{SD} = 30$ mm, $\phi = 5$ mm, $\mu_s = 10$ mm $^{-1}$, $g = 0.9$ ($\mu'_s = 1$ mm $^{-1}$), (Figure A8) $d_{SD} = 30$ mm, $\phi = 5$ mm, $\mu_s = 1$ mm $^{-1}$, $g = 0.0$ ($\mu'_s = 1$ mm $^{-1}$), (Figure A9) $d_{SD} = 40$ mm, $\phi = 1$ mm, $\mu_s = 1$ mm $^{-1}$, $g = 0.0$ ($\mu'_s = 1$ mm $^{-1}$), (Figure A10) $d_{SD} = 40$ mm, $\phi = 5$ mm, $\mu_s = 10$ mm $^{-1}$, $g = 0.9$ ($\mu'_s = 1$ mm $^{-1}$), (Figure A11) $d_{SD} = 40$ mm, $\phi = 5$ mm, $\mu_s = 1$ mm $^{-1}$, $g = 0.0$ ($\mu'_s = 1$ mm $^{-1}$).

We note that the depth z_0 of the banana in (A18) is different from the mean photon-visit depth $\langle z \rangle_{d_{SD}}$ and the reciprocal δ of the decay rate μ_{eff} , which are given by [29]

$$\langle z \rangle_{d_{SD}} = \frac{1}{2} \sqrt{d_{SD} \delta}, \quad \delta = \frac{1}{\mu_{\text{eff}}}, \quad (\text{A26})$$

where μ_{eff} is given in (14). In the case of $\mu_a = 0.01$ mm $^{-1}$, $\mu'_s = 1$ mm $^{-1}$ and $n = 1.4$, we have $z_0 = 5.7$ mm, $\langle z \rangle_{d_{SD}} =$

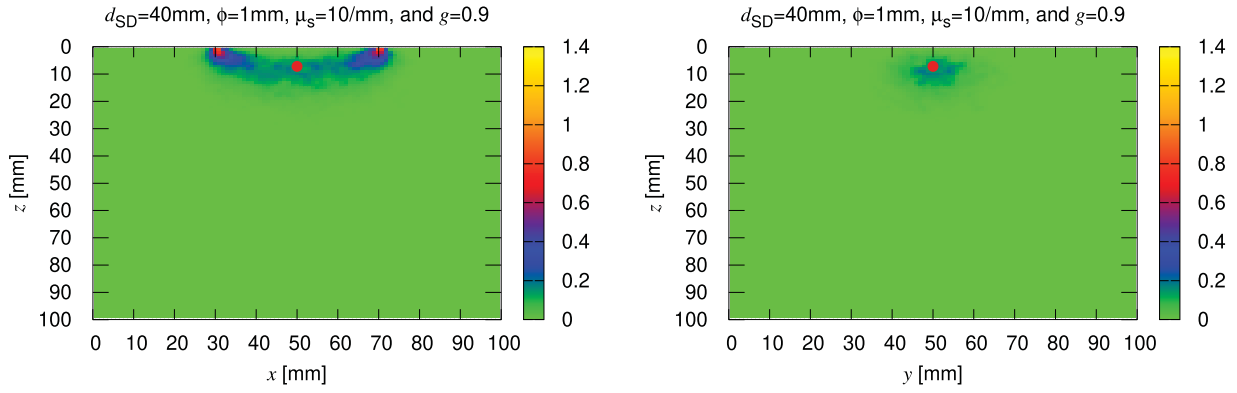


Figure A5. The spatial sensitivity profile is shown for $d_{SD} = 40$ mm, $\phi = 1$ mm, $\mu_s = 10$ mm $^{-1}$ and $g = 0.0$ ($\mu'_s = 1$ mm $^{-1}$). The cross sections at (Left) $y = 50$ mm and (Right) $x = 50$ mm are shown.

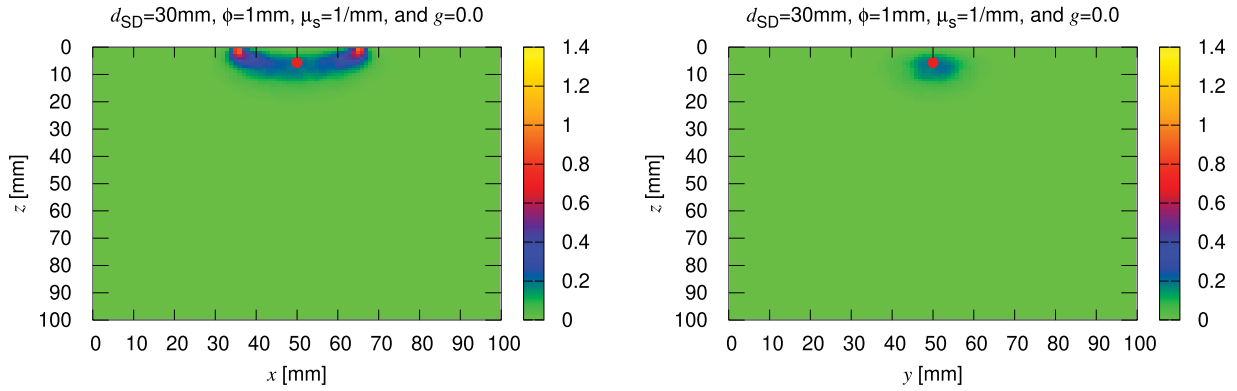


Figure A6. The spatial sensitivity profile is shown for $d_{SD} = 30$ mm, $\phi = 1$ mm, $\mu_s = 1$ mm $^{-1}$ and $g = 0.0$ ($\mu'_s = 1$ mm $^{-1}$). The cross sections at (Left) $y = 50$ mm and (Right) $x = 50$ mm are shown.

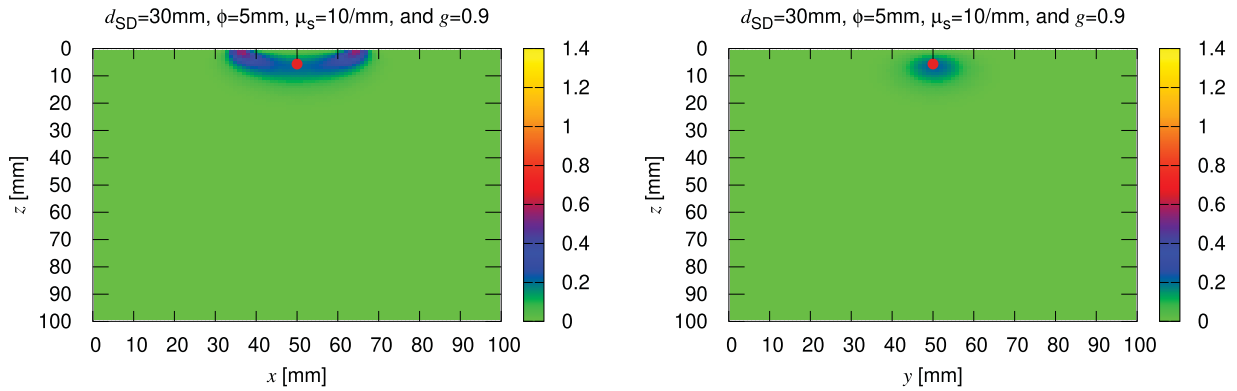


Figure A7. The spatial sensitivity profile is shown for $d_{SD} = 30$ mm, $\phi = 5$ mm, $\mu_s = 10$ mm $^{-1}$ and $g = 0.9$ ($\mu'_s = 1$ mm $^{-1}$). The cross sections at (Left) $y = 50$ mm and (Right) $x = 50$ mm are shown.

6.56 mm, $\delta = 5.74$ mm for $d_{SD} = 30$ mm, and $z_0 = 7.2$ mm, $\langle z \rangle_{d_{SD}} = 7.58$ mm, $\delta = 5.74$ mm for $d_{SD} = 40$ mm. We note that the formula (A26) was phenomenologically derived assuming $n \approx 1.36$.

The depth z_0 of the banana can be compared with the exponential decay of the spatially oscillating illumination with q_0 (i.e. frequency is $f = q_0/(2\pi)$). The specific intensity decays as $I \sim e^{-z/\xi_{q_0}}$, where $\xi_{q_0} = 1/\sqrt{3\mu_a\mu'_s + q_0^2}$ for small $\mu_a > 0$ [6,22]. For example, when $\mu'_s = 1$ mm $^{-1}$, $\mu_a = 0.01$ mm $^{-1}$, $q_0 = 1$ mm $^{-1}$ (i.e. $f = 0.16$ mm $^{-1}$), we have $\xi_{q_0} \approx 1$ mm. Since

$z_0 = 5.7$ mm for $d_{SD} = 30$ mm, we see $z_0 \gg \xi_{q_0}$. This motivates us to consider the stripe illumination, which is a structured illumination with the combination of spatial-frequency domain imaging and point-illumination imaging.

Appendix 2. Monte Carlo simulation

In Figures A6–A11, the position z_0 is compared with the spatial sensitivity profile from Monte Carlo simulation. The source-detector distance, diameter of optical fibres, scattering

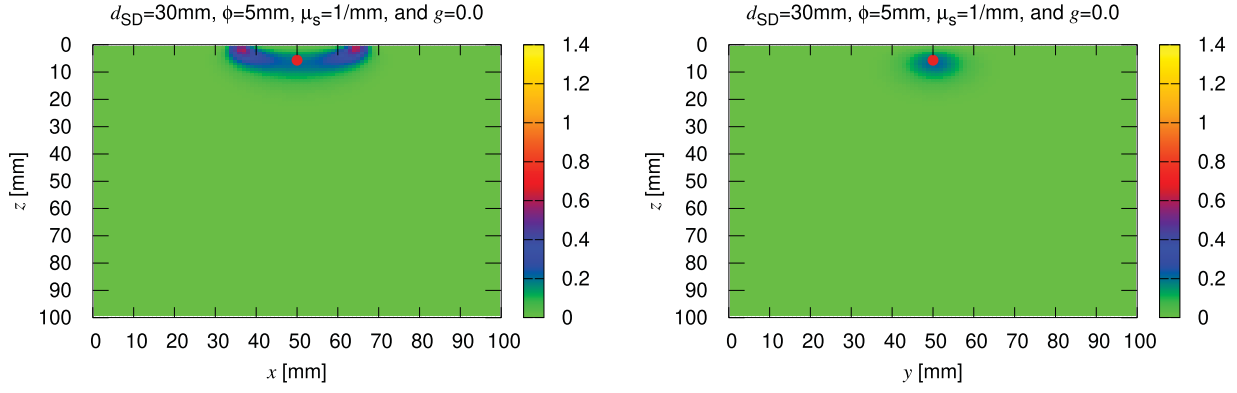


Figure A8. The spatial sensitivity profile is shown for $d_{SD} = 30$ mm, $\phi = 5$ mm, $\mu_s = 1$ mm $^{-1}$ and $g = 0.0$ ($\mu'_s = 1$ mm $^{-1}$). The cross-sections at (Left) $y = 50$ mm and (Right) $x = 50$ mm are shown.

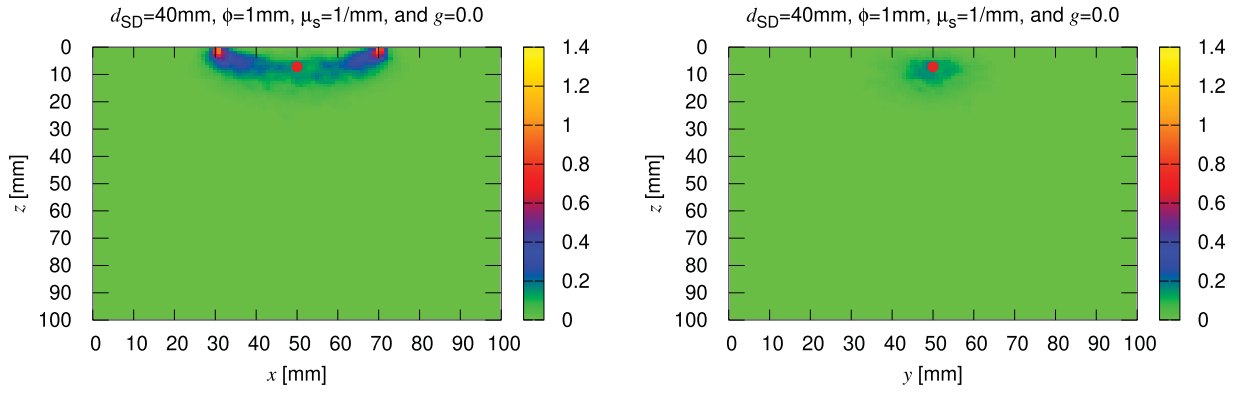


Figure A9. The spatial sensitivity profile is shown for $d_{SD} = 40$ mm, $\phi = 1$ mm, $\mu_s = 1$ mm $^{-1}$, and $g = 0.0$ ($\mu'_s = 1$ mm $^{-1}$). The cross-sections at (Left) $y = 50$ mm and (Right) $x = 50$ mm are shown.

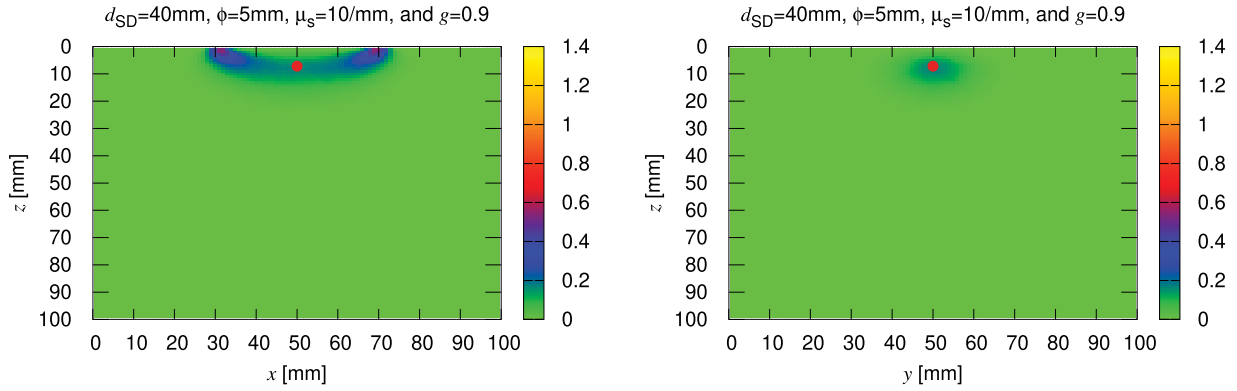


Figure A10. The spatial sensitivity profile is shown for $d_{SD} = 40$ mm, $\phi = 5$ mm, $\mu_s = 10$ mm $^{-1}$ and $g = 0.9$ ($\mu'_s = 1$ mm $^{-1}$). The cross-sections at (Left) $y = 50$ mm and (Right) $x = 50$ mm are shown.

coefficient, and anisotropic factor are denoted by d_{SD} , ϕ , μ_s and g , respectively.

Appendix 3. Green's function

Let us consider the Green's function which satisfies (A7). The Fourier transform is employed as

$$\tilde{G}(\mathbf{q}, z, \mathbf{r}') = \int_{\mathbb{R}^2} e^{-i\mathbf{q}\cdot\rho} G(\mathbf{r}, \mathbf{r}') d\rho, \quad (\text{A27})$$

where $\mathbf{q} \in \mathbb{R}^2$. We have

$$\begin{cases} \partial_z^2 \tilde{G} - \lambda(q)^2 \tilde{G} = \frac{-1}{D_0} e^{-i\mathbf{q}\cdot\rho'} \delta(z - z'), & z > 0, \\ -z_e \partial_z \tilde{G} + \tilde{G} = 0, & z = 0. \end{cases} \quad (\text{A28})$$

We can write

$$\tilde{G} = \begin{cases} A_1 e^{\lambda z} + A_2 e^{-\lambda z}, & 0 < z < z', \\ B e^{-\lambda z}, & z > z'. \end{cases} \quad (\text{A29})$$

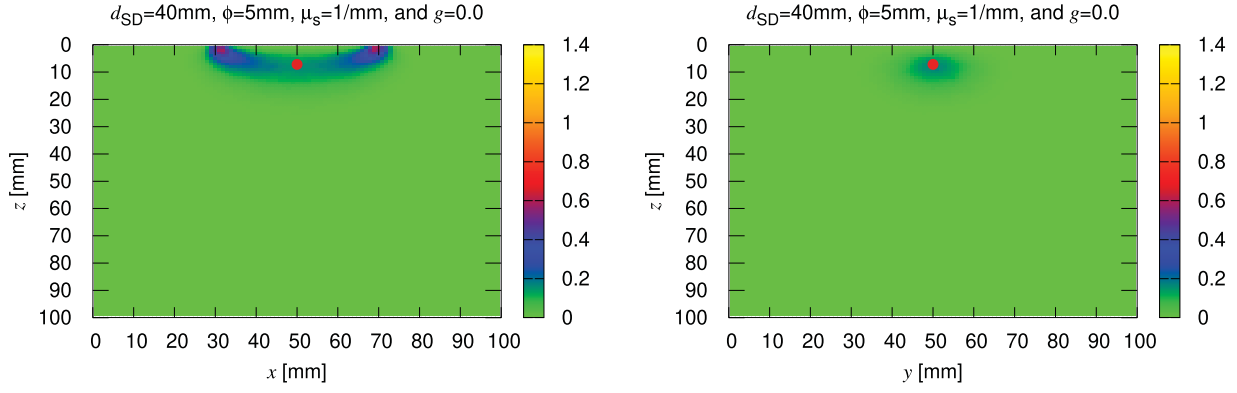


Figure A11. The spatial sensitivity profile is shown for $d_{SD} = 40$ mm, $\phi = 5$ mm, $\mu_s = 1$ mm $^{-1}$ and $g = 0.0$ ($\mu'_s = 1$ mm $^{-1}$). The cross-sections at (Left) $y = 50$ mm and (Right) $x = 50$ mm are shown.

We have

$$(1 - \lambda z_e)A_1 + (1 + \lambda z_e)A_2 = 0, \quad (\text{A30})$$

$$A_1 e^{\lambda z'} + A_2 e^{-\lambda z'} = B e^{-\lambda z'}, \quad (\text{A31})$$

and the jump condition

$$-B e^{-\lambda z'} - A_1 e^{\lambda z'} + A_2 e^{-\lambda z'} = \frac{-1}{\lambda D_0} e^{-iq \cdot \rho'}. \quad (\text{A32})$$

From the conditions (A30), (A31), and (A32), we obtain

$$\begin{aligned} A_1 &= \frac{1}{2\lambda D_0} e^{-iq \cdot \rho'} e^{-\lambda z'}, \\ A_2 &= \frac{z_e \lambda - 1}{z_e \lambda + 1} \frac{1}{2\lambda D_0} e^{-iq \cdot \rho'} e^{-\lambda z'}, \\ B &= \frac{1}{2\lambda D_0} e^{-iq \cdot \rho'} \left(e^{\lambda z'} + \frac{z_e \lambda - 1}{z_e \lambda + 1} e^{-\lambda z'} \right). \end{aligned} \quad (\text{A33})$$

Let $z' \rightarrow 0$. We obtain

$$\tilde{G}(\mathbf{q}, z, \mathbf{r}') = \frac{z_e}{D_0} e^{-iq \cdot \rho'} \frac{1}{z_e \lambda(q) + 1} e^{-\lambda(q)z}, \quad z > 0, z' = 0. \quad (\text{A34})$$

Therefore,

$$\begin{aligned} G(\mathbf{r}, \mathbf{r}') &= \frac{1}{(2\pi)^2} \int_{\mathbb{R}^2} e^{iq \cdot \rho} \tilde{G}(\mathbf{q}, z, \mathbf{r}') d\mathbf{q} \\ &= \frac{z_e}{(2\pi)^2 D_0} \int_{\mathbb{R}^2} e^{iq \cdot (\rho - \rho')} \frac{e^{-\lambda(q)z}}{1 + \lambda(q)z_e} d\mathbf{q}, \\ & \quad z > 0, z' = 0. \end{aligned} \quad (\text{A35})$$

We have

$$\begin{aligned} G(\mathbf{r}_0, \mathbf{r}_s) &= \frac{z_e}{(2\pi)^2 D_0} \int_{\mathbb{R}^2} e^{-iq_x(x_0 - x_s)} \frac{e^{-\lambda(q)z_0}}{1 + \lambda(q)z_e} d\mathbf{q} \\ &= \frac{z_e}{(2\pi)^2 D_0} \int_0^{2\pi} \int_0^\infty e^{-iq(x_0 - x_s) \cos \phi} \\ & \quad \times \frac{e^{-\lambda(q)z_0}}{1 + \lambda(q)z_e} q dq d\phi \\ &= \frac{z_e}{2\pi D_0} \int_0^\infty q J_0(q|x_0 - x_s|) \frac{e^{-\lambda(q)z_0}}{1 + \lambda(q)z_e} dq. \end{aligned} \quad (\text{A36})$$

Similarly we have

$$G(\mathbf{r}_0, \mathbf{r}_d) = \frac{z_e}{2\pi D_0} \int_0^\infty q J_0(q|x_0 - x_d|) \frac{e^{-\lambda(q)z_0}}{1 + \lambda(q)z_e} dq. \quad (\text{A37})$$

Appendix 4. Computation of H_ω

The function H_ω in (22) is written as

$$H_\omega(x, z, z') = \int_0^\infty F(q; x, z, z') dq, \quad (\text{A38})$$

where

$$\begin{aligned} F(q; x, z, z') &= \frac{1}{2\pi D_0 Q_\omega(q)} \cos(qx) \\ & \quad \times \left[e^{-Q_\omega(q)|z - z'|} - \frac{1 - Q_\omega(q)z_e}{1 + Q_\omega(q)z_e} e^{-Q_\omega(q)(z + z')} \right]. \end{aligned} \quad (\text{A39})$$

The integral can be evaluated by the double-exponential formula [38–40]. Define

$$\phi(\tau) = \frac{\tau}{1 - e^{-6 \sinh \tau}} \quad (\text{A40})$$

with

$$\phi'(\tau) = \frac{1 - (1 + 6\tau \cosh \tau) e^{-6 \sinh \tau}}{(1 - e^{-6 \sinh \tau})^2}. \quad (\text{A41})$$

We have

$$\begin{aligned} & \int_0^\infty F(q; x, z, z') dq \\ & \approx \frac{\pi}{|x|} \sum_{k=-N_k}^{N_k} F\left(\frac{\pi}{|h|x|} \phi\left(kh + \frac{h}{2}\right); x, z, z'\right) \\ & \quad \times \phi'\left(kh + \frac{h}{2}\right), \end{aligned} \quad (\text{A42})$$

where $N_k > 0$ is an integer and h is a mesh size.

Appendix 5. Pseudoinverse

Let us consider

$$\boldsymbol{\eta} = \mathbf{J}_{\text{reg}}^+ \boldsymbol{\psi}. \quad (\text{A43})$$

C.1. Underdetermined

In this case,

$$J_{\text{reg}}^+ = J_-^* M_{\text{reg}}^{-1}, \quad \underline{M} = J J_-^*. \quad (\text{A44})$$

Here, * denotes the Hermitian conjugate and reg means that the pseudoinverse is regularized by discarding singular values that are smaller than σ_0 . Let σ_j^2 and \mathbf{v}_j be the eigenvalues and eigenvectors of the matrix \underline{M} :

$$\underline{M} \mathbf{z}_j = \sigma_j^2 \mathbf{z}_j. \quad (\text{A45})$$

We obtain

$$\boldsymbol{\eta} = \sum_{\substack{j \\ \sigma_j > \sigma_0}} \frac{1}{\sigma_j^2} (\mathbf{z}_j^* \boldsymbol{\psi}) J_-^* \mathbf{z}_j. \quad (\text{A46})$$

C.2. Overdetermined

In this case,

$$J_{\text{reg}}^+ = M_{\text{reg}}^{-1} J_-^*, \quad \underline{M} = J_-^* J. \quad (\text{A47})$$

After solving the eigenproblem $\underline{M} \mathbf{z}_j = \sigma_j^2 \mathbf{z}_j$, we obtain

$$\boldsymbol{\eta}_1 = \sum_{\substack{j \\ \sigma_j > \sigma_0}} \frac{1}{\sigma_j^2} (\mathbf{z}_j^* J_-^* \boldsymbol{\psi}) \mathbf{z}_j. \quad (\text{A48})$$